IEEE Access
Multidisciplinary | Rapid Review | Open Access Journal

Date of current version 13 June, 2024.

Digital Object Identifier 10.1109/ACCESS.2024.?

Novel Electromagnetic-Based Radar Propagation Model for Vehicular Sensing

FRANÇOIS DE SAINT MOULIN[1], KHALDOUN AL KHALIFEH[1], CHRISTOPHE CRAEYE[1] (Senior Member, IEEE), LUC VANDENDORPE[1], (Fellow, IEEE), and CLAUDE OESTGES[1] (Fellow, IEEE)

[1]ICTEAM, UCLouvain, Louvain-la-Neuve, Belgium

e-mail: firstname.lastname@uclouvain.be

François De Saint Moulin is a Research Fellow of the Fonds de la Recherche Scientifique - FNRS.

ABSTRACT With the increased carrier frequencies envisioned for future radar and communication systems, transmissions in the near-field propagation region have raised an increased interest. In order to evaluate the performance of such systems, accurate propagation models are required to predict efficiently the received powers at each node, and draw correct conclusions. In this paper, we develop new radar propagation models based on ElectroMagnetic (EM) theory, helping to clarify in which cases popular models from the literature, namely the radar equation and the Geometrical Optics (GO) approximation, are valid. The target is modelled as a flat square or curved rectangular plate, enabling to compute analytically the scattered EM fields, and evaluate accurate Radar Cross-Sections (RCS). With a flat plate, the novel model directly highlights the link between the radar equation and the GO approximation, used e.g. in ray-tracing applications. Radar cross-section measurements are then performed in order to validate the models with multiple target geometries, e.g. square plates, sphere and cylinder. Finally, the impact of such modelling is evaluated by considering popular automotive scenarios, within the stochastic geometry framework.

INDEX TERMS electromagnetism, propagation, path-loss, radar, vehicular, radar cross-section, stochastic geometry

I. INTRODUCTION

Radar and communication systems both exploit the EM spectrum with specific objectives. On the one hand, radar systems are deployed in order to gather information about the environment by transmitting a known waveform. By receiving and processing the waveform echoes created by multiple targets, the radar system is able to estimate multiple parameters such as the position, speed and angle of the targets. On the other hand, communication systems are deployed in order to transmit information to other systems in an unknown environment, which is usually also estimated in order to compensate for the generated impairments.

Usually, radar waveforms are transmitted at high carrier frequencies, namely the 24 GHz band for automotive applications [1], while communication waveforms are transmitted at lower carrier frequencies, namely from 410 MHz up to 5.9 GHz for the Long Term Evolution (LTE) frequency bands. In recent years, higher frequency bands have been considered for both radar and communication functions. For example, the 77-81 GHz frequencies has become the new standard for recent automotive radar systems [1]. Similarly, the 5G New Radio standard extends previous standards to cover new spectrum offering up to 7.125 GHz in a first instance, and then frequencies from 24.25 GHz up to 71 GHz [2]. In this context, both radar and communication systems are converging towards the same frequencies, leading to an increased interest in joint radar-communication technologies. Moreover, with the frequency increase, the Fraunhofer distances associated to many popular scenarios increase from meters to multiple hundred of meters. This implies that, at such wavelengths, most transmissions occur in the near-field propagation region, requiring to adapt the considered propagation models.

Therefore, in order to design radar and communication systems, new radar and communication propagation models are required, in view of the targeted applications. These models are then used to estimate the received radar echoes and communication signals powers, directly impacting the performance of both systems. Their accuracy is therefore crucial in order to draw reliable conclusions about the system performance, for instance by means of stochastic geometry, a popular framework to obtain closed-form expressions of average performance metrics in large-scale wireless networks [3]–[5]. This applies to any work where the radar echo power is analysed, such as [6] or [7]. In the former, the radar interference is assumed to decrease with the fourth power of the distance. As shown in this paper, this may not always be the case. The latter consider a vehicular network, in which the radar targets is assumed to have a constant RCS. Again, it is shown in this paper that the RCS may vary with the distance.

A. CLASSICAL RADAR AND COMMUNICATION PROPAGATION MODELS

First, for communication applications, the *Friis equation* yields at the power P_{C} received from a transmit node at a distance R as [8]

$$P_{\mathrm{C}}(R) = \mathrm{EIRP}\; G_r\, \frac{c^2}{4\pi f_c^2}\, \beta^{-1}\, R^{-\alpha}, \tag{1}$$

where EIRP denotes the transmitted Effective Isotropic Radiated Power, G_r is the receive beamforming gain, and f_c is the carrier frequency. A linear path-loss model is considered, with β the fixed intercept and α the path-loss exponent. For free-space propagation, $\beta = 4\pi$ and $\alpha = 2$.

Instead, for radar applications, the received power P_{R} is usually computed following the *radar equation* [9]:

$$P_{\mathrm{R,RE}}(R) = \mathrm{EIRP}\; G_r\, \frac{c^2}{4\pi f_c^2}\, \beta^{-2}\, R^{-2\alpha}\, \sigma, \tag{2}$$

with σ the RCS of the target. The RCS is usually supposed to be constant. However, the modelling of the RCS is difficult, and often inaccurate. Additionally, this is only valid in the far-field, i.e. when $r >> R_{\mathrm{F}} = 2D^2\, f_c/c$ with R_{F} the Fraunhofer distance, and D the largest dimension of the scatterer. In many recent applications, e.g. automotive scenarios, this assumption is not always fulfilled. This can lead to significantly wrong conclusions about the achieved performance. Another model for the received power is based on the GO approximation, which is for instance used in ray-tracing applications [10]. In that case, the received power is expressed as

$$P_{\mathrm{R,GO}}(R) = \mathrm{EIRP}\; G_r\, \frac{c^2}{4\pi f_c^2}\, \beta^{-1}\, (2R)^{-\alpha}\, |\mathcal{R}|^2, \tag{3}$$

where $\mathcal{R}$ is the Fresnel reflection coefficient. Assuming a good conductor, one may assume that $|\mathcal{R}|^2 \approx 1$. The GO approximation is similar to (1), in which the receiver would be located at a distance $2R$. However, owing to the GO approximation, the dimensions and shapes of the targets are not explicitly taken into account, as the EM waves are approximated with rays.

B. APPLICATIONS IN STOCHASTIC GEOMETRY

Within the stochastic geometry framework, for radar applications, [11] analyses the cumulative distribution function of the interference with multiple pulsed-radar devices, [12] evaluates the detection probability when multiple obstacles are distributed around the radar systems, and [13], [14] study the radar performance achieved in a cluttered environment. This framework is also specifically used to analyse automotive scenarios. As a non-exhaustive list, [15] evaluates the performance achieved for different RCS models. Multiple lanes are considered in [16] and [17], the former equipped with front- and side-mounted radars with directional antenna patterns, and the latter taking into account the interference from reflections on vehicles in the neighbouring lanes. Instead of using Poisson point processes to model the nodes positions, [18] uses a one-dimensional lattice, and [19], [20] uses Matérn hard-core processes, respectively in one or two dimensions. Fine-grained analysis is applied in [21], [22] to evaluate the meta distribution of the Signal to Interference-plus-Noise Ratio (SINR), enabling to analyse the reliability of the detection at each individual vehicle. Recently, joint radar and communication (radcom) applications have also been considered. For automotive applications [23] and [24] evaluate the cooperative detection range of the system, respectively with spectrum allocation between both functions or with a joint system.

In all these works, the radar equation is extensively used to model the received radar echo power. A constant RCS is assumed, irrespective of the target shape and dimensions, the distance, or the carrier frequency. However, this might yield misleading conclusions, especially in radcom scenarios, where (1) and (2) are respectively used to model the interference and the radar echo power. Thus, new radar propagation and RCS models are needed to improve the accuracy and relevance of the performance analysis.

C. NEAR-FIELD RADAR CROSS-SECTION

The analysis of the RCS in the near-field region is not a new topic. In the XX$^{\text{th}}$ century, [25] already showed that the RCS of a sphere and a square plate in the near-field region is dependent of the range and orientation of the antennas. It proposed two new definitions of the RCS in the near-field, as variations of the radar equation. The monostatic and bistatic RCS in the near-field is already analysed through a Physical Optics (PO) approach in [26]. It also gives numerical examples for rectangular and circular plates. This work has been extended in [27], where complex targets are decomposed into small triangular elements, such that each element propagates in the far-field. A similar approach is proposed in [28].

Following these works, multiple papers have analysed near-field RCSs. Namely, [29] and [30] compare numerical simulations and measurements for rectangular plates with an oblique incidence at 24 GHz. Other simple targets are analysed in [31] and [32]. Respectively circular plates and cylinder are evaluated numerically for the former, and sphere and cylinder are studied, numerically and with measurements, at 5.24 GHz for the latter. The RCS of complex targets, i.e. the back of a car at 77 GHz, are evaluated in [33]. From another perspective, [34] proposes to use RCS model of [32] to develop a procedure extracting the scattering matrix coefficients of the targets using analogue beamforming.

Nonetheless, owing to the complexity of the RCS computation, most of these works focus on numerical analysis and measurements. Instead, [35] proposes three-dimensional computationally efficient models based on Fresnel integrals to calculate the backscattering model of a rectangular plate. It also compares these models to measurements at 28 GHz. This work is further extended in [36], which leverages on the proposed models to evaluate the backscattered fields with multiple oriented rectangular surfaces.

D. CONTRIBUTIONS

The contributions of this paper are summarised as follows:

- Analytical radar propagation and RCS models are re-developed for a flat square plate target, based on the EM theory, and more precisely the PO approximation. The extension to rectangular target is also straightforward. These models are valid for propagations occurring either in the near- or far-field region. Additionally, they unify the radar equation and the GO approximation, showing that the former is suited for far-field applications if the RCS is assumed to be constant, whereas the latter is appropriate for near-field scenarios. Moreover, a simple closed-form approximation of the RCS is also proposed, enabling to simplify the model. The approximation is especially accurate for high carrier frequencies, and thus performs well for automotive radar applications.
- The analytical radar propagation and RCS models obtained for a flat square plate target are extended to curved rectangular plate geometries. The shape of the target can arbitrarily be defined as a continuous 3D surface. The obtained model shows that the curvature of the target around the specular reflection point, i.e. the second derivatives of the shape function, defines the behaviour of the RCS with the distance and carrier frequency. Moreover, a simple closed-form approximation of the RCS is again proposed to simplify the model.
- RCS measurements are performed to validate the proposed models with five different geometries: square plates of different dimensions (5, 10, and 100 cm), a sphere (diameter of 55 cm), and a cylinder (diameter of 15 cm, height of 100 cm). Excellent results are obtained for the square plate of 10 cm, with errors smaller than 0.5 dB for frequencies between 16 and 23 GHz. Nevertheless, larger discrepancies are observed for the other geometries (especially with the curved targets). Yet, they enable to highlight the impact of the target geometry on the RCS variations, with the distance and carrier frequency, as modelled analytically by the proposed models.
- The new propagation models are applied to an automotive scenario analysed within the stochastic geometry framework, in order to evaluate the impact of the choice of the model on the achieved performance. Significant differences are observed depending on the choice of the model and the parametrisation, showing that the latter should be specifically chosen regarding the considered scenario.

E. STRUCTURE OF THE PAPER

First, EM theory is used in Section II to compute the scattered fields for targets modelled as flat square and curved rectangular plates. From the scattered fields, propagation and RCS models are derived, the links between the new models, the radar equation and the GO approximation are detailed, and numerical analyses are performed. Then, new EM-based radar propagation models are proposed in Section III, extending the results of Section II to arbitrary path-loss models. Next, the new models are applied to an automotive scenario within the stochastic geometry framework in Section IV to observe the impact of the propagation model on the evaluation of the achieved radar performance. Finally, RCS measurements are performed in Section V to validate the theoretical models, and highlight the dependency of the RCS with the distance, the carrier frequency, and the target geometry.

II. ELECTROMAGNETIC REFLECTION IN FREE-SPACE

In this section, the EM theory is used in order to compute the scattered electric field, considering first a flat, and then a curved Perfect Electric Conductor (PEC) square plate target. In order to obtain these results, the Stationary Phase Approximation (SPA) is first introduced in Section II-A. Knowing the incident EM fields, described in Section II-B, the scattered electric field is then computed in Section II-C for a flat square plate, in the near-field, far-field, and at the limit between the two regions. The results are next extended for curved rectangular targets in Section II-D. Finally, a numerical analysis is performed in Section II-E.

A. STATIONARY PHASE APPROXIMATION

The SPA is a useful method to approximate the integral of a rapidly oscillating function [37]. Let us consider a 1D integral written as

$$I = \int_{\Omega} g(x)\, e^{j\psi(x)}\, \mathrm{d}x, \tag{4}$$

where g is a function to integrate on the domain Ω, and ψ a given phase function. The SPA consists in approximating the phase of ψ by a Taylor expansion around a stationary phase x_0, defined such that $\psi'(x_0) = 0$, and assumed to be located within Ω:

$$\psi(x) = \psi(x_0) + \frac{1}{2}\,\psi''(x_0)(x - x_0)^2 + \mathcal{O}(x^3). \tag{5}$$

Assuming that the amplitude function g varies slowly compared to the phase function ψ in the vicinity of x_0, the integral can be approximated as

$$I \approx g(x_0)\, e^{j\psi(x_0)} \int_{\Omega} e^{j\frac{1}{2}\psi''(x_0)(x-x_0)^2}\, \mathrm{d}x. \tag{6}$$

Furthermore, if the value of $\psi''(x_0)$ is sufficiently large with respect to the boundaries of Ω, such that the integration domain contains multiple oscillations of the phase function, the second-order term of the phase rapidly oscillates, leading to successive cancellations. In that case, the integration boundaries can be extended to infinity without affecting significantly the result, and the integral can be approximated as

$$I \approx g(x_0)\, e^{j\psi(x_0)} \sqrt{\frac{j\,2\pi}{\psi''(x_0)}}. \tag{7}$$

Note that, even for limited integration domains, (6) is still valid if the amplitude function varies slowly compared to the complete integration domain. In that case, the integral can be solved using the (normalised) *Fresnel integral*, defined as [38]

$$F(x) \triangleq \int_0^x e^{j\pi \frac{t^2}{2}}\, \mathrm{d}t. \tag{8}$$

Let us denote three arbitrary parameters by $A, B, C \in \mathbb{C}$. One can leverage on (8) to perform the following integration:

$$\int_A^B e^{-jCt^2}\, \mathrm{d}t = D\left[F^*\left(\frac{B}{D}\right) - F^*\left(\frac{A}{D}\right)\right], \tag{9}$$

with $D \triangleq \sqrt{\pi/2C}$. Additionally, knowing that $F(-x) = -F(x)$, when $A = -B$, one obtains the following relation:

$$\int_{-B}^B e^{-jCt^2}\, \mathrm{d}t = 2D\,F^*\left(\frac{B}{D}\right). \tag{10}$$

B. INCIDENT ELECTROMAGNETIC FIELDS

Let us assume that the transmitting antenna is a linear antenna, such that the transmitted electric and magnetic fields at a distance R' of the antenna can be written as

$$\vec{E}_i = -jk\eta LI\, \frac{e^{-jkR'}}{4\pi R'}\, f(\theta)\, \hat{e}_\theta, \tag{11}$$

$$\vec{H}_i = \frac{1}{\eta}\, \hat{e}_r \times \vec{E}_i = -jkLI\, \frac{e^{-jkR'}}{4\pi R'}\, f(\theta)\, \hat{e}_\phi. \tag{12}$$

In these equations, $k = 2\pi/\lambda$ is the wave number with λ the wavelength, $\eta = 377\ \Omega$ is the free-space impedance, L is the antenna length, I is the current flowing through the antenna, assumed to be constant, $f(\theta)$ is the normalised antenna radiation pattern, with θ the elevation angle, equal to 0° when the direction of propagation is parallel to the antenna. The normalised antenna radiation pattern is assumed to be maximum when $\theta = 0^\circ$. A polar coordinate system is associated to the antenna, with $\hat{e}_r$, $\hat{e}_\theta$, and $\hat{e}_\phi$ being respectively the radial, elevation and azimuth unit vectors. These vectors are illustrated in Figure 1.

Equations (11) and (12) are valid when $R >> 2L^2/\lambda$, which is rewritten as $R >> \lambda$ when the antenna length is not much larger than the wavelength. Owing to the considered frequencies for actual radar systems (up to 81 GHz), this condition is always fulfilled in the considered scenarios.

C. FLAT SQUARE PLATE TARGET

Let us first consider the scenario illustrated in Figure 1. The coordinate system is defined such that a linear antenna located

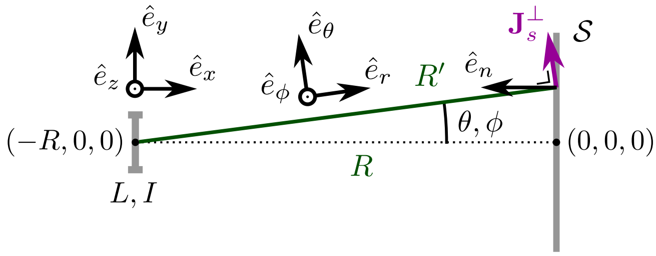

FIGURE 1: Flat square plate geometry.

at $(-R, 0, 0)$ is facing a square plate $\mathcal{S}$ of dimension D, defined as

$$\mathcal{S} \triangleq \left\{ (x, y, z) \in \mathbb{R}^3 \,\middle|\, x = 0,\ |y| \le \frac{D}{2},\ |z| \le \frac{D}{2} \right\}. \tag{13}$$

The normal unit vector pointing towards the antennas is given by $\hat{e}_n = -\hat{e}_x$. The spherical coordinate system associated to the antenna is defined as

$$\begin{bmatrix} \hat{e}_r \\ \hat{e}_\theta \\ \hat{e}_\phi \end{bmatrix} \triangleq \begin{bmatrix} \cos\theta\cos\phi & \sin\theta & \cos\theta\sin\phi \\ -\sin\theta\cos\phi & \cos\theta & -\sin\theta\sin\phi \\ -\sin\phi & 0 & \cos\phi \end{bmatrix} \begin{bmatrix} \hat{e}_x \\ \hat{e}_y \\ \hat{e}_z \end{bmatrix}, \tag{14}$$

with ϕ the azimuth angle. One can compute angles θ and ϕ from the (x, y, z)-coordinates as

$$\sin\phi = \frac{z}{\sqrt{(R+x)^2 + z^2}}, \quad \sin\theta = \frac{y}{\sqrt{(R+x)^2 + y^2 + z^2}},$$
$$\cos\phi = -\frac{R+x}{\sqrt{(R+x)^2 + z^2}}, \quad \cos\theta = \frac{\sqrt{(R+x)^2 + z^2}}{\sqrt{(R+x)^2 + y^2 + z^2}}. \tag{15}$$

Following the PO approximation, the equivalent electric surface current density generated at the surface of the plate can be computed from (12) as

$$\vec{J}_s = 2\,\hat{e}_n \times \vec{H}_i = -2jkLI\, \frac{e^{-jkR'}}{4\pi R'}\, f(\theta)\, \cos\phi\, \hat{e}_y, \tag{16}$$

with $R' \triangleq \sqrt{R^2 + y^2 + z^2}$. The component of the current density perpendicular to the direction of propagation is then computed as

$$\begin{aligned} \vec{J}_s^\perp &= \vec{J}_s - (\vec{J}_s \cdot \hat{e}_r)\, \hat{e}_r \\ &= -2jkLI\, \frac{e^{-jkR'}}{4\pi R'}\, f(\theta)\, \cos\phi\, [\hat{e}_y - (\hat{e}_y \cdot \hat{e}_r)\, \hat{e}_r] \\ &= -2jkLI\, \frac{e^{-jkR'}}{4\pi R'}\, f(\theta)\, \cos\phi\, \cos\theta\, \hat{e}_\theta. \end{aligned} \tag{17}$$

The backscattered electric field is then approximated from (16) as

$$\begin{aligned} \vec{E}_s &\approx -jk\eta \int_{\mathcal{S}} \vec{J}_s^\perp\, \frac{e^{-jkR'}}{4\pi R'}\, \mathrm{d}\mathcal{S} \\ &= -\frac{k^2\eta LI}{8\pi^2} \int_{\mathcal{S}} \frac{f(\theta)\, \cos\phi\, \cos\theta}{R'^2}\, e^{-\jmath 2kR'}\, \hat{e}_\theta\, \mathrm{d}\mathcal{S}. \end{aligned} \tag{18}$$

In (18), one can distinguish the amplitude and phase functions, defined as

$$\vec{g}(R', \theta, \phi) \triangleq \frac{f(\theta)\, \cos\phi\, \cos\theta}{R'^2}\, \hat{e}_\theta, \tag{19}$$

$$\psi(R') \quad \triangleq -2kR'. \tag{20}$$

Both functions can be rewritten w.r.t. the position $(0, y, z)$ on the plate. For the phase function, one obtains

$$\psi(y,z) = -2k\sqrt{R^2 + y^2 + z^2}. \tag{21}$$

1) Solution in the Near-Field

In the near-field region, the SPA may be applied to solve (18). The stationary point, which is also the specular reflection point, is located at the centre of the plate. The amplitude and phase functions are approximated as

$$\vec{g}(y,z) \approx \vec{g}(R,0,0) = \frac{1}{R^2}\,\hat{e}_y, \tag{22}$$

$$\psi(y,z) \approx -2kR - k\,\frac{y^2+z^2}{R}. \tag{23}$$

Following the developments of Section II-A, on the one hand, the amplitude function is assumed to not vary significantly around the stationary point. On the other hand, the phase function is approximated by a Taylor expansion around the stationary point. Still, in order to apply (7), the target must be large enough to contain multiple Fresnel zones [39]. Quantitatively, the m^{th} Fresnel zones radius ρ_m is computed from the phase function as

$$\frac{k}{R}\,\rho_m^2 = m\,\frac{\pi}{2} \quad\Leftrightarrow\quad \rho_m = \frac{1}{2}\sqrt{m\lambda R}, \tag{24}$$

with $m \in \mathbb{N}$. Therefore, for a square plate of dimension $D \geq \rho_m$ with m sufficiently large, the conditions holds for distances R such that

$$R << \frac{D^2}{m\lambda} = \frac{R_\text{F}}{2m}. \tag{25}$$

Thus, the approximation given in (7) can only be applied for distances sufficiently small compared to the Fraunhofer distance of the target, i.e. in the near-field region of the target.

Consequently, in the near-field, the scattered electric field of (18) is approximated as

$$\begin{aligned}\vec{E}_s &\approx -\frac{k^2\eta LI}{8\pi^2}\,\frac{1}{R^2}\,e^{-j2kR}\,\frac{-j\pi R}{k}\,\hat{e}_y\\ &= jk\eta LI\,\frac{e^{-jk(2R)}}{4\pi(2R)}\,\hat{e}_y.\end{aligned} \tag{26}$$

By comparing (26) to (11), one may notice that the scattered electric field is equivalent to the electric field which would have been received by an antenna located at a distance $2R$ of the transmitting antenna, with a phase shift of 180° owing to the PEC. The scattered power density is computed as

$$S_s = \frac{|\vec{E}_s|^2}{2\eta} = \frac{\text{EIRP}}{4\pi(2R)^2}, \tag{27}$$

where $\text{EIRP} = k^2\eta L^2 I^2/8\pi$. Multiplying this equation by the effective area of the receive antenna, the resulting power corresponds to the GO approximation in free-space, presented in (3). Moreover, this is also valid if the transmit and receive antennas are not aligned with the centre of the plate, as long as the specular reflection point, and multiple Fresnel zones around this point, are still included within the plate.

2) Solution in the Far-Field

Instead, in the far-field, for the carrier frequencies usually considered in radar applications, the distance R is large such that

$$R >> R_\text{F} = \frac{2D^2}{\lambda} >> y^2 + z^2, \quad \forall (y,z) \in \mathcal{S}. \tag{28}$$

Thus, the phase function can be approximated with a Taylor series as

$$\begin{aligned}\psi(y,z) &= -2kR\sqrt{1+\frac{y^2+z^2}{R^2}}\\ &\approx -2kR\left(1+\frac{y^2+z^2}{2R^2}\right),\end{aligned} \tag{29}$$

giving back (23). Additionally, since the plate dimension is small compared to the distance between the antennas and the target, one can assume that $R' \approx R$, $\theta \approx 0°$, and $\phi \approx 0°$ in the amplitude function, giving back (22). Thus, the same approximations for the amplitude and phase functions are obtained both in the near- and far-field. Nonetheless, the condition of (25) is not fulfilled. Consequently, (7) cannot be applied to solve the integral. Injecting (22) and (23) in (18) leads to the following expression of the backscattered field:

$$\vec{E}_s \approx -\frac{k^2\eta LI}{8\pi^2}\,\frac{1}{R^2}\,e^{-j2kR}\left(\int_{-\frac{a}{2}}^{\frac{a}{2}} e^{-jk\frac{u^2}{R}}\,\mathrm{d}u\right)^2\hat{e}_y. \tag{30}$$

This integral must be solved using the Fresnel functions.

3) Solution with Fresnel Functions

As described in Section II-A, if the distance R is large such that the first Fresnel zones are not contained within the plate, the integral of (30) can still be solved with (6) instead of (7). Thus, the scattered electric field is approximated as

$$\begin{aligned}\vec{E}_s &\approx -\frac{k^2\eta LI}{8\pi^2}\,\frac{1}{R^2}\,e^{-j2kR}\left(\int_{-\frac{a}{2}}^{\frac{a}{2}} e^{-jk\frac{y^2}{R}}\,\mathrm{d}y\right)^2\hat{e}_y\\ &\overset{(a)}{=} -\frac{k^2\eta LI}{8\pi^2}\,\frac{1}{R^2}\,e^{-j2kR}\,\frac{2\pi R}{k}\left(F^*\left(\sqrt{\frac{2k}{\pi R}}\frac{D}{2}\right)\right)^2\hat{e}_y\\ &= -k\eta LI\,\frac{e^{-jk(2R)}}{4\pi(2R)}\,\Upsilon\left(\frac{R}{R_\text{F}}\right)\hat{e}_y,\end{aligned} \tag{31}$$

where equality (a) is obtained using (10), and the function Υ, illustrated in Figure 2, is defined as

$$\Upsilon(x) \triangleq 2\left(F^*\left(\sqrt{\frac{1}{2x}}\right)\right)^2. \tag{32}$$

Note that, if the transmit and receive antennas are not aligned with the centre of the plate, one may use (9) instead of (10), leading to similar results. The applications of these developments for rectangular plates is also straightforward. Moreover, for tilted plates, a rotation of the coordinate system can be considered, the problem thus reducing to the case where the antennas are unaligned with the centre of the plate.

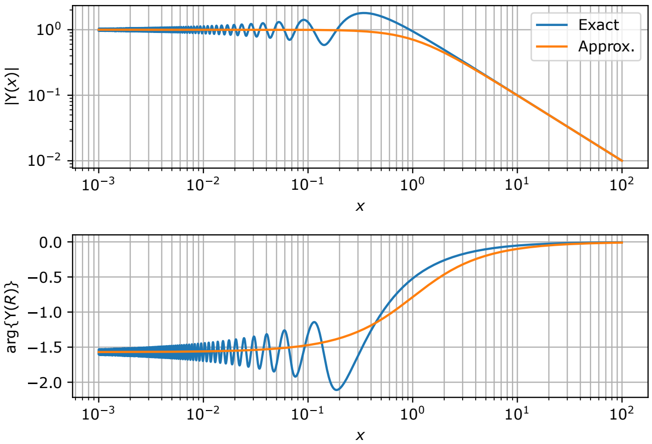

FIGURE 2: Modulus and angle of the function Υ, and approximation of (38).

The solution with Fresnel functions is valid for propagation in both the near- and far-field regions. The function Υ has the following properties:

$$\lim_{x\to 0} \Upsilon(x) = -j, \tag{33}$$

$$\lim_{x\to\infty} \Upsilon(x) = \frac{1}{x}. \tag{34}$$

Consequently, in the near-field, one may inject (33) in (31), giving back (26). Contrariwise, in the far-field, one may inject (34) in (31), leading to

$$\vec{E}_s \approx -k\eta LI \frac{e^{-jk(2R)}}{8\pi R^2} R_\mathrm{F}\, \hat{e}_y. \tag{35}$$

The corresponding scattered power density is then computed as

$$S_s = \frac{\left|\vec{E}_s\right|^2}{2\eta} = \frac{\mathrm{EIRP}}{(4\pi R^2)^2} \pi R_\mathrm{F}^2. \tag{36}$$

Multiplying this equation by the effective area of the receive antenna, the resulting power corresponds to the radar equation in free-space, presented in (2), assuming that the RCS is modelled as $\sigma = \pi R_\mathrm{F}^2$.

4) Approximation of the Fresnel Function

The asymptotic behaviour of the function Υ, described by (33) and (34), is similar to the asymptotic behaviour of a low-pass filter. Consequently, in order to approximate the normalised Fresnel integral defined in (8), while keeping the asymptotic properties of the function, the following approximation is proposed empirically:

$$F(x) \approx \left(\frac{1}{x^2} - 2j\right)^{-\frac{1}{2}}. \tag{37}$$

Injecting this approximation in (32), one obtains the following approximation for the function Υ:

$$\Upsilon(x) \approx \frac{x-j}{1+x^2}. \tag{38}$$

This expression is represented in Figure 2. The properties given in (33) and (34) still hold. Yet, it enables to simplify the model and filter the oscillatory behaviour of the function Υ. Moreover, the modulus of Υ is approximated as

$$|\Upsilon(x)| \approx \left(\frac{1}{1+x^2}\right)^{\frac{1}{2}}. \tag{39}$$

Such approximation for the modulus may be extended for any natural number $n \geq 2$ to reduce the transition region, giving

$$|\Upsilon(x)| \approx \left(\frac{1}{1+x^n}\right)^{\frac{1}{n}}. \tag{40}$$

5) Radar Cross-Section Model

On the one hand, the incident power density at the centre of the plate is computed from (11) as

$$S_i = \frac{\left|\vec{E}_i\right|^2}{2\eta} = \frac{\mathrm{EIRP}}{4\pi R^2}. \tag{41}$$

where $\mathrm{EIRP} = k^2\eta L^2 I^2/8\pi$. On the other hand, the scattered power density for both near- and far-field propagations is computed from (31) as

$$S_s = \frac{\left|\vec{E}_s\right|^2}{2\eta} = \frac{\mathrm{EIRP}}{4\pi(2R)^2} \left|\Upsilon\left(\frac{R}{R_\mathrm{F}}\right)\right|^2. \tag{42}$$

The RCS is then evaluated as follows:

$$\sigma \triangleq 4\pi R^2 \frac{S_s}{S_i} = \pi R^2 \left|\Upsilon\left(\frac{R}{R_\mathrm{F}}\right)\right|^2. \tag{43}$$

Asymptotically, in the near- and far-field, this can be simplified using (33) and (34) as

$$\sigma \approx \begin{cases} \pi R^2 & \text{if } R << R_\mathrm{F}, \\ \pi R_\mathrm{F}^2 = 4\pi|\mathcal{S}|/\lambda^2 & \text{if } R >> R_\mathrm{F}, \end{cases} \tag{44}$$

where $|\mathcal{S}|$ is the surface of the plate. Thus, this highlights that the RCS is constant in the far-field, as obtained in (36), while it is a function of the distance in the near-field. Using the approximation of (40), the RCS is approximated as

$$\sigma \approx \sigma_0\, \tilde{\sigma}(R). \tag{45}$$

where $\sigma_0 \triangleq \pi R_\mathrm{F}^2$, and $\tilde{\sigma}$ is a distance-dependent factor, which may be introduced in the radar equation to model the variation of the RCS with the distance for flat square targets:

$$\tilde{\sigma}(R) \triangleq \left[1 + \left(\frac{R_\mathrm{F}}{R}\right)^n\right]^{-\frac{2}{n}}. \tag{46}$$

6) Summary

In summary, the radar equation and GO approximation should be selected to model the radar propagation depending on the dimension of the target, and the distance between the antennas and the target. On the one hand, when the target is large such that the reflection propagates in the near-field, the received power is well modelled with the GO approximation. On the other hand, when the target is small such that the reflection propagates in the far-field, the RCS is constant, and the radar

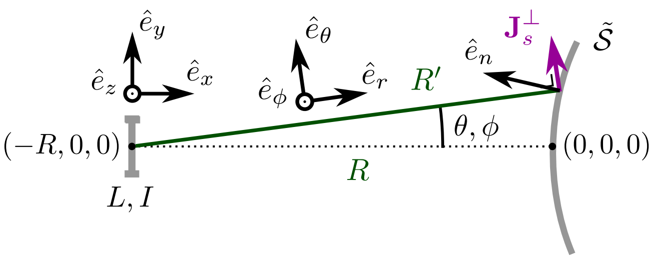

FIGURE 3: Curved square plate geometry.

equation is suited to model the radar propagation. Yet, the radar equation can be applied in any case, if the RCS is modelled as a distance-dependent quantity in the near-field. For instance, the new model of (43) can model the RCS in both the near- and far-field regions, but also in the transition between the two regions.

D. CURVED SQUARE PLATE TARGET

Let us now consider the scenario illustrated in Figure 3. The coordinate system is defined such that a linear antenna located at $(-R, 0, 0)$ is facing a curved rectangular plate $\tilde{S}$ of dimension D_y and D_z. The shape of the curved plate is modelled through a well-behaved arbitrary function $h : \mathbb{R} \times \mathbb{R} \to \mathbb{R}$ as:

$$\tilde{S} \triangleq \left\{ (x, y, z) \in \mathbb{R}^3 \;\middle|\; \begin{array}{l} x = h(y, z),\ |y| \leq \dfrac{D_y}{2},\ |z| \leq \dfrac{D_z}{2} \\ h(0, 0) = 0, \quad \nabla h(0, 0) = 0 \\ \nabla^2 h(y, z) \succeq 0,\ \dfrac{\partial^2 h}{\partial y \partial z}(0, 0) = 0 \end{array} \right\}. \tag{47}$$

The last condition ensures that the principal directions of the target are aligned with the coordinate system. It is also assumed that the function h varies slowly w.r.t. the wavelength. The same spherical coordinate system and angles, described in (14) and (15), are defined. However, the distance R' is now defined as

$$R' \triangleq \sqrt{(R + h(y, z))^2 + y^2 + z^2}. \tag{48}$$

Moreover, the normal unit vector pointing outside the curved plate is now given by

$$\hat{e}_n = \frac{-\hat{\mathbf{e}}_x + \frac{\partial h}{\partial y}\,\hat{\mathbf{e}}_y + \frac{\partial h}{\partial z}\,\hat{\mathbf{e}}_z}{\sqrt{1 + \left(\frac{\partial h}{\partial y}\right)^2 + \left(\frac{\partial h}{\partial z}\right)^2}}. \tag{49}$$

Thus, the equivalent electric surface current density is expressed as

$$\vec{J}_s = 2\,\hat{e}_n \times \vec{H}_i = -2jkLI\,\frac{e^{-jkR'}}{4\pi R'}\,f(\theta)\,(\hat{e}_n \times \hat{e}_\phi), \tag{50}$$

and the backscattered electric field is computed as

$$\begin{aligned} \vec{E}_s &\approx -jk\eta \int_{\tilde{S}} \vec{J}_s^\perp\,\frac{e^{-jkR'}}{4\pi R'}\,\mathrm{d}\tilde{S} \\ &= -\frac{k^2\eta LI}{8\pi^2} \int_{\tilde{S}} \frac{f(\theta)}{R'^2}\,e^{-\jmath 2kR'}\,\hat{e}_u\,\mathrm{d}\tilde{S}, \end{aligned} \tag{51}$$

with

$$\hat{e}_u \triangleq (\hat{e}_n \times \hat{e}_\phi) - [(\hat{e}_n \times \hat{e}_\phi) \cdot \hat{e}_r]\,\hat{e}_r. \tag{52}$$

In (51), one can again distinguish the amplitude and phase functions, defined as

$$\vec{g}(R', \theta, \phi) \triangleq \frac{f(\theta)}{R'^2}\,\hat{e}_u, \tag{53}$$

$$\psi(R') \triangleq -2kR'. \tag{54}$$

1) Solution with Fresnel Functions

In the case of curved surfaces, the stationary point is found by solving

$$\begin{cases} y + [R + h(y, z)]\,\dfrac{\partial h}{\partial y}(y, z) = 0 \\ z + [R + h(y, z)]\,\dfrac{\partial h}{\partial z}(y, z) = 0. \end{cases} \tag{55}$$

The solution of this system of equation is not straightforward. Nonetheless, following the Fermat stationary point theorem [40], the stationary point minimises the total travelled distance. It follows geometrically that $(y_0, z_0) = (0, 0)$. This is confirmed mathematically by entering in (55) the properties of the function h defined in (47). Still using these properties, the second derivatives of the phase function are given by

$$\frac{\partial^2 \psi}{\partial y^2}(0, 0) = -\frac{2k}{R}\left[1 + R\,\frac{\partial^2 h}{\partial y^2}(0, 0)\right], \tag{56}$$

$$\frac{\partial^2 \psi}{\partial z^2}(0, 0) = -\frac{2k}{R}\left[1 + R\,\frac{\partial^2 h}{\partial z^2}(0, 0)\right], \tag{57}$$

$$\frac{\partial^2 \psi}{\partial y \partial z}(0, 0) = 0. \tag{58}$$

Thus, denoting by h_y'' and h_z'' the second derivatives of h w.r.t. y and z at the origin, the phase function can be approximated around the stationary point as

$$\psi(y, z) \approx -2kR - \frac{k}{R}\left[1 + Rh_y''\right] y^2 - \frac{k}{R}\left[1 + Rh_z''\right] z^2. \tag{59}$$

Regarding the amplitude function, the approximation of (22) is obtained again around the stationary point.

Consequently, defining

$$R_y \triangleq \frac{R}{1 + Rh_y''}, \qquad R_z \triangleq \frac{R}{1 + Rh_z''}, \tag{60}$$

the scattered electric field of (51) is approximated as

$$\begin{aligned} \vec{E}_s &\approx -\frac{k^2\eta LI}{8\pi^2}\,\frac{1}{R^2}\,e^{j2kR} \int_{-\frac{D}{2}}^{\frac{D}{2}} e^{-j\frac{k}{R_y}y^2}\,\mathrm{d}y \int_{-\frac{D}{2}}^{\frac{D}{2}} e^{-j\frac{k}{R_z}z^2}\,\mathrm{d}z \\ &= -\frac{k^2\eta LI}{8\pi^2}\,\frac{1}{R^2}\,e^{j2kR}\,\frac{2\pi}{k}\sqrt{R_yR_z} \\ &\qquad \cdot F^*\left(\sqrt{\frac{2k}{\pi R_y}}\,\frac{D_y}{2}\right) F^*\left(\sqrt{\frac{2k}{\pi R_z}}\,\frac{D_z}{2}\right)\hat{e}_y \\ &= -k\eta LI\,\frac{\sqrt{R_yR_z}}{8\pi R^2}\,e^{j2kR}\sqrt{\Upsilon\left(\frac{R_y}{R_{\mathrm{F},y}}\right)\Upsilon\left(\frac{R_z}{R_{\mathrm{F},z}}\right)}\,\hat{e}_y, \end{aligned} \tag{61}$$

where the Fraunhofer distances $R_{\mathrm{F},y}$ and $R_{\mathrm{F},z}$ associated to each dimension of the rectangular plate are defined as

$$R_{\mathrm{F},y} \triangleq \frac{2D_y^2}{\lambda}, \quad R_{\mathrm{F},z} \triangleq \frac{2D_z^2}{\lambda}. \tag{62}$$

2) Radar Cross-Section Model

With a curved target, the scattered power density is computed from (61) as

$$S_s = \frac{\left|\vec{E}_s\right|^2}{2\eta} = \frac{\mathrm{EIRP}}{16\pi R^2}\frac{R_y R_z}{R^2}\left|\Upsilon\left(\frac{R_y}{R_{\mathrm{F},y}}\right)\Upsilon\left(\frac{R_z}{R_{\mathrm{F},z}}\right)\right|. \tag{63}$$

The RCS is then evaluated as follows:

$$\sigma \triangleq 4\pi R^2 \frac{S_s}{S_i} = \pi R_y R_z \left|\Upsilon\left(\frac{R_y}{R_{\mathrm{F},y}}\right)\Upsilon\left(\frac{R_z}{R_{\mathrm{F},z}}\right)\right|, \tag{64}$$

and it may be approximated using (40) as

$$\sigma \approx \sigma_0\, \tilde{\sigma}(R), \tag{65}$$

where $\sigma_0 \triangleq \pi R_{\mathrm{F},y} R_{\mathrm{F},z}$, and $\tilde{\sigma}$ is again a distance-dependent factor, which may be introduced in the radar equation to model the variation of the RCS with the distance for curved square targets:

$$\tilde{\sigma}(R) \triangleq \left[\left(1+\left(\frac{R_{\mathrm{F},y}}{R_y}\right)^n\right)\left(1+\left(\frac{R_{\mathrm{F},z}}{R_z}\right)^n\right)\right]^{-\frac{1}{n}}. \tag{66}$$

Let us analyse the impact of the curvature by considering a square target of dimension $D_y = D_z = D$, with the same curvature in both the y- and z-dimensions, i.e. $h_y'' = h_z'' = h''$. We define the *curvature radius* as $c \triangleq 1/h''$. One may already notice that

(i) when $c \geq R_{\mathrm{F}}$, i.e. for small curvatures, the curvature does not impact significantly the RCS, compared to a flat target. For $R << R_{\mathrm{F}}$, $R_y = R_z \approx R$, and following (33), $\sigma \approx \pi R^2$. For $R >> R_{\mathrm{F}}$, following (34), $\sigma \approx \pi R_{\mathrm{F}}^2$;

(ii) when $c << R_{\mathrm{F}}$, i.e. for large curvatures, the curvature has a significant impact on the RCS, compared to a flat target. For distance $R >> c$, even in the near-field, $R_y = R_z \approx c$, and the RCS already converges to a constant value, approximately equal to $\sigma \approx \pi c^2 \left|\Upsilon(c/R_{\mathrm{F}})\right|^2$.

3) Application to Specific Shapes

Let us consider three specific shapes, namely the cylinder, the sphere, and the paraboloid.

a: Cylinder of radius ρ

With a cylinder of radius $\rho >> D_y$, curved along the z-dimension, the function h is defined as

$$h(y,z) = \rho - \sqrt{\rho^2 - z^2}. \tag{67}$$

The curvatures h_y'' and h_z'', and the distances R_y and R_z in the y- and z-axis are thus given by

$$h_y'' = 0 \quad \Rightarrow \quad R_y = R, \tag{68}$$

$$h_z'' = \frac{1}{\rho} \quad \Rightarrow \quad R_z = \left(\frac{1}{R}+\frac{1}{\rho}\right)^{-1}. \tag{69}$$

b: Sphere of radius ρ

With a sphere of radius $\rho >> \max(D_y, D_z)$, the function h is defined as

$$h(y,z) = \rho - \sqrt{\rho^2 - y^2 - z^2}. \tag{70}$$

The curvatures h_y'' and h_z'', and the distances R_y and R_z in the y- and z-axis are thus given by

$$h_y'' = h_z'' = \frac{1}{\rho} \quad \Rightarrow \quad R_y = R_z = \left(\frac{1}{R}+\frac{1}{\rho}\right)^{-1}. \tag{71}$$

c: Paraboloid

With a paraboloid of curvature radii $c_y >> \max(D_y, D_z)$ and $c_z >> \max(D_y, D_z)$ in the y- and z-axis, the function h is defined as

$$h(y,z) = \frac{y^2}{2c_y} + \frac{z^2}{2c_z}. \tag{72}$$

The curvatures h_y'' and h_z'', and the distances R_y and R_z in the y- and z-axis are thus given by

$$h_y'' = \frac{1}{c_y} \quad \Rightarrow \quad R_y = \left(\frac{1}{R}+\frac{1}{c_y}\right)^{-1}, \tag{73}$$

$$h_z'' = \frac{1}{c_z} \quad \Rightarrow \quad R_z = \left(\frac{1}{R}+\frac{1}{c_z}\right)^{-1}. \tag{74}$$

From the paraboloid, the results obtained with a cylinder of radius ρ are matched if $c_y = 0$ and $c_z = \rho$, and the results obtained with a sphere of radius ρ are matched if $c_y = c_z = \rho$.

E. NUMERICAL ANALYSIS

Figure 4 illustrates the evolution of the RCS with the distance for different carrier frequencies (5 GHz for WiFi frequencies, 24 GHz and 77 GHz for automotive radars) and different curvature radii, computed with (64), or with (65) using the approximation of the modulus of the function Υ. The higher the carrier frequency, the better the modulus approximation. It enables to filter out the oscillatory behaviour of the Fresnel functions, while keeping the trend of the RCS. However, at low carrier frequencies, when a constant RCS is reached, an offset is observed with the approximation for curved targets.

Compared to the flat target geometry, introducing curvatures in the y- and z-axis modifies drastically the behaviour of the RCS:

(i) when $c_y << R_{\mathrm{F},y}$, $c_y << R$, $c_z << R_{\mathrm{F},z}$, $c_z << R$, the RCS is constant, whatever the Fraunhofer distance;

(ii) when $c_y << R << c_z$ (resp. $c_z << R << c_y$), the RCS is proportional to the distance, until the Fraunhofer distance of the z-axis (resp. y-axis) is reached;

(iii) when $R << c_y$ and $R << c_z$, the RCS is proportional to the square of the distance, until the Fraunhofer distances are reached. This is the case corresponding to the flat target.

At high carrier frequencies, the Fraunhofer distances are high compared to the considered distances in indoor applications. This is also often the case in automotive scenarios. Therefore, the modelling of the target has a significant impact

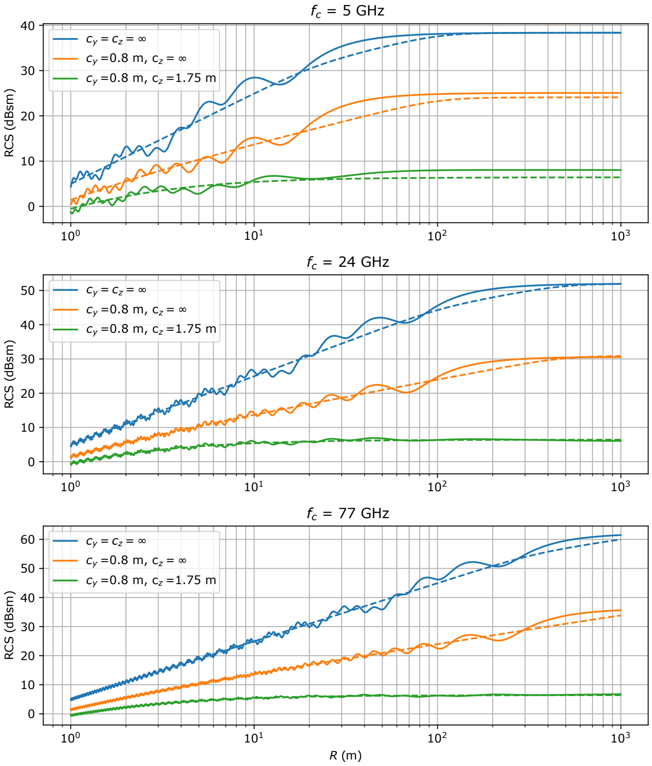

FIGURE 4: RCS against distance for different carrier frequencies and different curvature radii. Infinite curvature radii correspond to a flat plate. The dashed lines represent the approximation obtained using (65) with $n = 4$. Carrier frequencies of 5, 24 and 77 GHz corresponds to Fraunhofer distances of 33, 160, and 510 m.

on the radar propagation model. The RCS is either constant, proportional to the distance, or proportional to the square of the distance, depending on the considered range, frequency, and target geometry.

III. ELECTROMAGNETIC-BASED RADAR PROPAGATION MODEL WITH ARBITRARY PATH-LOSS

In Section II, the link between the radar equation and the GO approximation has been highlighted. A novel RCS model for flat or curved geometries, in the near- and far-field, has been proposed in (65). Thus, the equivalent radar propagation model is written as

$$P_{\mathrm{R}}(R) = \mathrm{EIRP}\ G_r\, \frac{c^2}{4\pi f_c^2}\, \frac{\sigma_0}{(4\pi)^2}\, \frac{\tilde{\sigma}(R)}{R^4}, \tag{75}$$

where $\sigma_0 \triangleq \pi R_{\mathrm{F},y} R_{\mathrm{F},z}$, and $\tilde{\sigma}$ is defined in (66). The radar equation (with constant RCS) and the GO approximation models are particular cases of this general model.

These models can also be generalised to be compatible with any path-loss model with fixed intercept β and path-loss exponent α. In that case, the definition of the RCS is adapted

TABLE 1: Parameters of the scenario.

Parameters	Value
Vehicles density	10 km^{-1}
Plate dimensions	$D_y = D_z = 1$ m
Number of lanes	5
Lanes width	3.6 m
Interference probability	0.01
Path-loss parameters	$\beta = 4\pi$, $\alpha = 2$
Carrier frequency	76.5 GHz
EIRP	10 dB
Receiver gain	$G_r = 30$ dBi
Antenna beamwidth	15°
SINR threshold	$\kappa = 10dB$

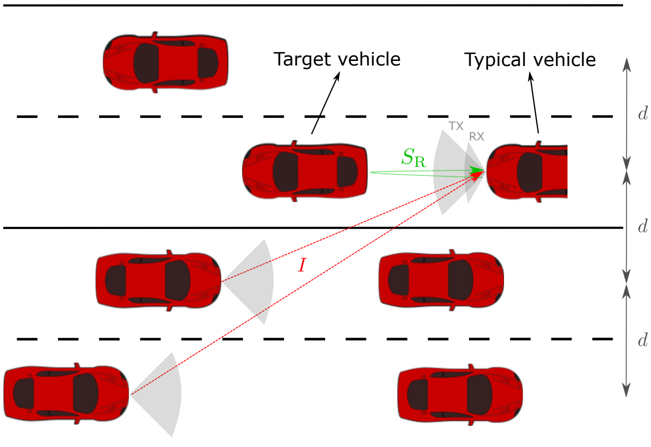

FIGURE 5: Multi-lane automotive scenario.

as

$$\sigma \triangleq \beta R^{\alpha} \left(\frac{S_s}{S_i}\right)^{\frac{\alpha}{2}} = \frac{\beta (R_y R_z)^{\frac{\alpha}{2}}}{2^{\alpha}} \left| \Upsilon\left(\frac{R_y}{R_{\mathrm{F},y}}\right) \Upsilon\left(\frac{R_z}{R_{\mathrm{F},z}}\right)\right|^{\frac{\alpha}{2}}, \tag{76}$$

and it may be approximated using (40) as

$$\begin{aligned}\sigma &\approx \frac{\beta (R_y R_z)^{\frac{\alpha}{2}}}{2^{\alpha}} \left[\left(1 + \left(\frac{R_y}{R_{\mathrm{F},y}}\right)^{n}\right)\left(1 + \left(\frac{R_{\mathrm{F},z}}{R_{\mathrm{F},z}}\right)^{n}\right)\right]^{-\frac{\alpha}{2n}} \\ &= \sigma_0\, \tilde{\sigma}(R),\end{aligned} \tag{77}$$

where $\sigma_0 \triangleq \beta \left(R_{\mathrm{F},y} R_{\mathrm{F},z}\right)^{\frac{\alpha}{2}} / 2^{\alpha}$, and the distance-dependent factor $\tilde{\sigma}$ is defined as

$$\tilde{\sigma}(R) \triangleq \left[\left(1 + \left(\frac{R_{\mathrm{F},y}}{R_y}\right)^{n}\right)\left(1 + \left(\frac{R_{\mathrm{F},z}}{R_z}\right)^{n}\right)\right]^{-\frac{\alpha}{2n}}. \tag{78}$$

The equivalent radar propagation model is finally written as

$$P_{\mathrm{R}}(R) = \mathrm{EIRP}\ G_r\, \frac{c^2}{4\pi f_c^2}\, \frac{\sigma_0}{\beta^2}\, \frac{\tilde{\sigma}(R)}{R^{2\alpha}}. \tag{79}$$

IV. APPLICATION TO AN AUTOMOTIVE SCENARIO WITHIN THE STOCHASTIC GEOMETRY FRAMEWORK

In this section, the different radar propagation models developed in Sections II and III are compared within the stochastic geometry framework, following the scenario studied in [15].

In that paper, the authors study the performance of automotive radar systems in a bidirectional multi-lane street, as illustrated by Figure 5. One typical vehicle receives simultaneously a radar echo of power P_R from the next vehicle ahead, and a total interference I from the vehicles driving on the opposite lanes. The interference power is modelled using the Friis equation, while the radar equation is used to compute the radar echo power. Instead of simply consider a constant RCS, they model fluctuation by introducing a χ^2-distributed random variable, as suggested in the Swerling I and III models [41]. Random fluctuation models can be coupled with the proposed radar propagation models by including the RCS model of (65) as the average RCS of the random variable distributions. The performance metric is the *radar success probability*, defined as the probability that the radar SINR is higher than a given SINR threshold κ for a given distance. Denoting by W the noise power, it is written as

$$P_\mathrm{D}(R) \triangleq \mathbb{P}\left(\frac{P_\mathrm{R}(R)}{I+W} > \kappa\right). \tag{80}$$

In this work, the considered parameters for the scenario are summarised in Table 1.

Figure 6 illustrates the success probability achieved with (79) assuming a constant RCS of 30 dBsm, or a distance-dependent RCS, using the GO approximation, or the new models with flat or curved targets. The impact of the approximation of the function Υ proposed in (40) is also illustrated. This radar propagation model is combined either with the Swerling I (exponential distribution), or the Swerling V (constant value) RCS fluctuations models. One can observe that the selected radar propagation model hugely affects the radar performance owing to the significant differences of received power, related to the dependency of the RCS with the distance. Additionally, among the new models, the choice of the curvature radii has also an important impact on the achieved performance. Whereas a flat square plate seems appropriate for trucks, the introduction of a curvature radius in the vertical dimension seems more suited to cars, and leads to a large performance degradation. The GO model is close to the flat square model since a high carrier frequency is considered, leading to a high Fraunhofer distance compared to the radar-to-target distance. Additionally, for the selected configuration, the model with a constant RCS of 30 dBsm also approximates well the model with vertical curvature radius. Finally, the proposed approximation for the function Υ enables to efficiently filter out the oscillations of the average RCS. These oscillations may not be relevant for the evaluation of average performance in the stochastic geometry framework, owing to the high level of abstraction.

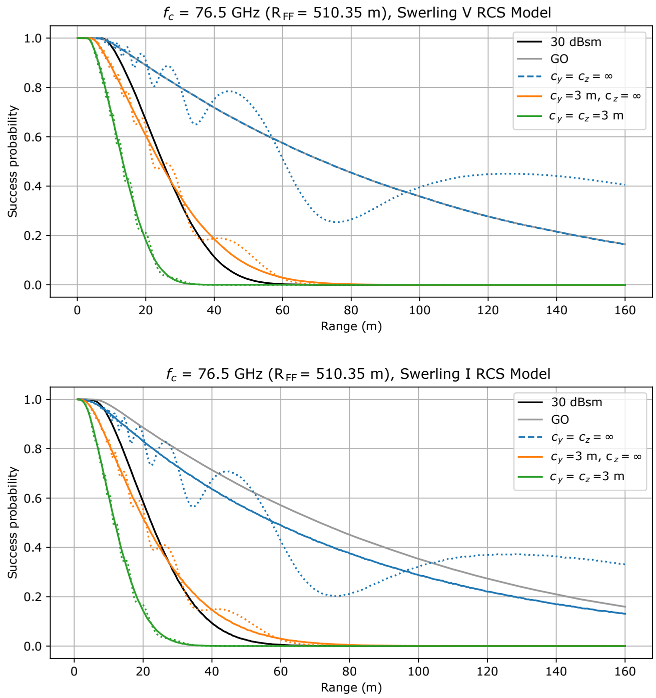

FIGURE 6: Success probability achieved with the multiple radar propagation models of (3) (gray), (2) (black), and (79) with different curvature radii (other colors). The dotted lines correspond to the full RCS model proposed in (76), and the solid line correspond to the approximation with the distance-depend factor given in (78). Swerling I (exponential distribution), and Swerling V (constant value) RCS fluctuation models are respectively considered in the bottom and top figures.

V. RADAR CROSS-SECTION MEASUREMENTS

RCS measurements have been performed in the anechoic chamber of the WELCOME facility at UCLouvain. The five targets of Figure 7a are considered:

(i) A flat square plate of dimension $D \times D = 5 \times 5$ cm,
(ii) A flat square plate of dimension $D \times D = 10 \times 10$ cm,
(iii) A flat square plate of dimension $D \times D = 1 \times 1$ m,
(iv) A cylinder of height $D_y = 1$ m and radius $\rho = 15$ cm,
(v) A sphere of radius $\rho = 27.5$ cm.

In the following, we respectively refer to the square targets as the small square plate (SSP), medium square plate (MSP), and large square plate (LSP).

The measurements are performed using a Vector Network Analyser (VNA) PNA-X N5242B from Keysight, which enables to obtain the transmittance matrix between two inputs at frequencies up to 26.5 GHz, with a transmit power up to 10 dBm. This power level is sufficient for the considered targets to obtain echoes higher than the noise floor, at the considered Intermediate Frequency (IF) bandwidth of 100 Hz. Thus, no amplifier is used, to avoid any additional source of errors. The antennas are two H-A26-W15 horns from RF Spin, operating at frequencies from 18 to 26.5 GHz. A zoom on the VNA and the antennas is shown in Figure 7b. Note that additional absorbing foam is put between the VNA and the antennas during the measurements, to limit the impact of reflections on the VNA for targets with high RCSs.

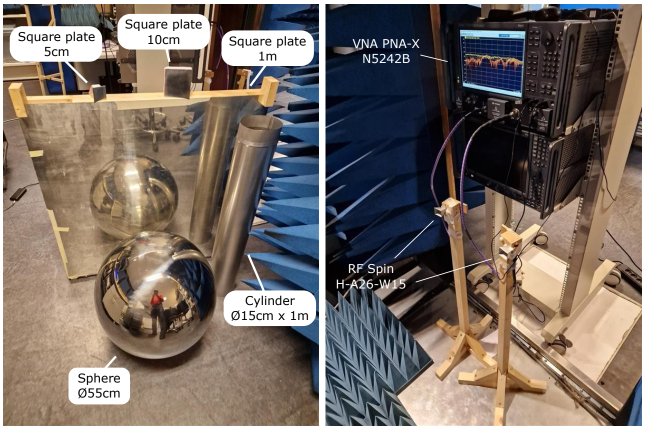

(a) Targets (b) VNA and horn antennas

FIGURE 7: Considered target geometries, VNA PNA-X N5242B from Keysight, and horn antennas H-A26-W15 from RF spin, used for RCS measurements.

A. MEASUREMENT OF THE ANTENNAS GAIN

First, the antennas gain has been measured using the setup shown in Figure 8. Denoting by S_{ant} the transmittance between the output and the input of the VNA, the antennas gain G_{ant} at a given frequency is computed following the Friis equation of (1) in free-space as

$$[G_{\text{ant}}(f)]_{\text{dB}} = 20\log_{10}|S_{\text{ant}}(f)| - 20\log_{10}\left(\frac{c}{4\pi f\, R_{\text{ant}}}\right), \tag{81}$$

with $R_{\text{ant}} = 45$ cm the distance between the two antennas and c the speed of light. A 2-port calibration is carried out with the cables only, so that the cable losses can be calibrated out.

B. MEASUREMENT OF THE RADAR CROSS-SECTION

The measurement setup is shown in Figure 9 for the MSP. Additional absorbing foam is put in front of the boxes under the small targets to avoid undesirable reflections. Moreover, as described before, it is also inserted between the antennas and the VNA for large targets, as the echo from the target is powerful enough to reflect a second time on the VNA.

For each target geometry and distance, the clutter transmittance S_{clut} is first measured by performing a measurement with the target removed from the experimental setup, and it is saved in the memory of the VNA. Next, the transmittance S is measured with the target, and the background is removed by the VNA. Thus, the data $S - S_{\text{clut}}$ is extracted for post-processing.

C. POST-PROCESSING

The received data consists on 501 points in the frequency domain between 15 and 25 GHz (by steps of 20 MHz). The signal is first converted in time domain. Then, it is filtered with a 41-points Hamming window, centred on the peak of the dominant path. This enables to further isolate the target re-

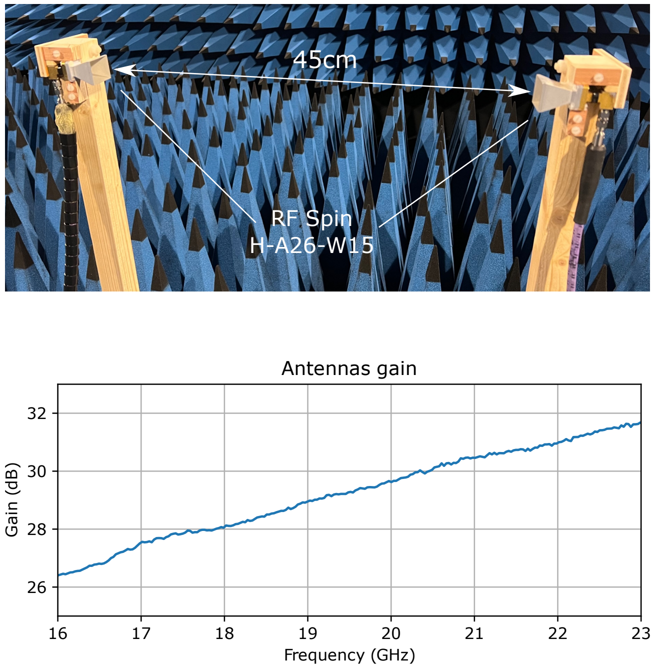

FIGURE 8: Measurement of the antennas gain — setup and result.

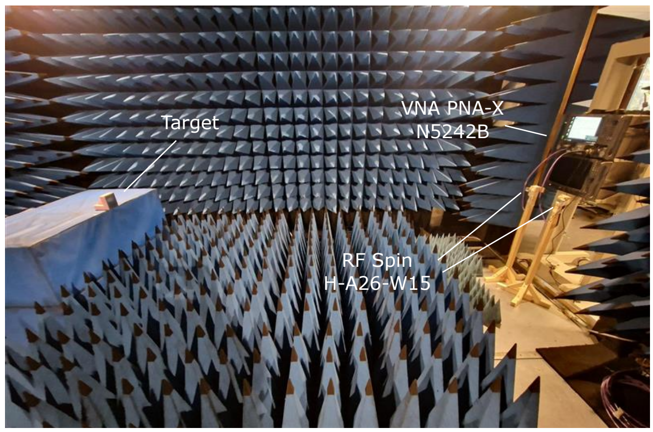

FIGURE 9: RCS measurement setup for the flat square plate target of 10 cm.

sponse. Next, the RCS σ is obtained from the post-processed data, denoted $\tilde{S}$, by computing

$$[\sigma]_{\text{dB}} = 20\log_{10}\left|\tilde{S}(f)\right| - [G_{\text{ant}}(f)]_{\text{dB}} - [\gamma(f)]_{\text{dB}}\,, \tag{82}$$

with γ defined by the radar equation as

$$\gamma(f) = \frac{c^2}{(4\pi)^3 f^2 R^4}, \tag{83}$$

where R is the distance between the target and the centre of the line connecting both antennas.

D. RESULTS

The RCS measurements performed for the five targets of Figure 7a are shown in Figure 10. All the measurements are

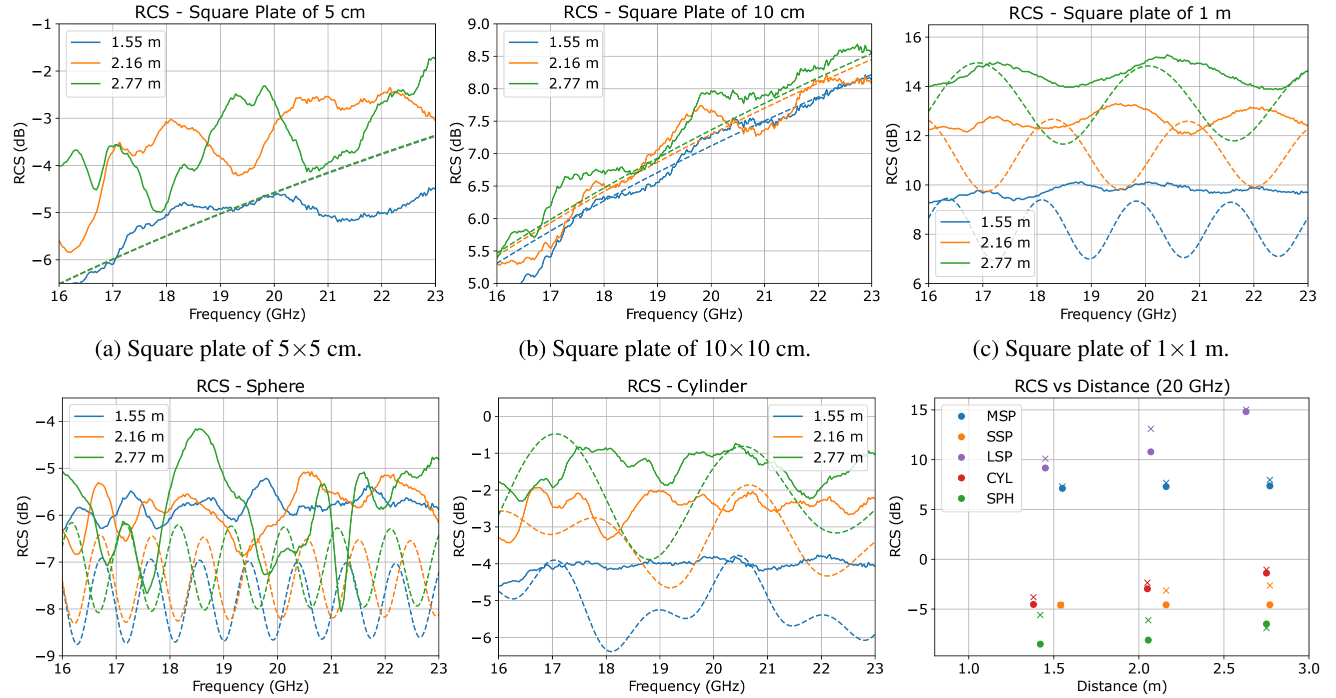

(a) Square plate of 5×5 cm. (b) Square plate of 10×10 cm. (c) Square plate of 1×1 m.

(d) Sphere with 55 cm diameter. (e) Cylinder of 1 m with 15 cm diameter. (f) RCS against distance for $f_c = 20$ GHz.

FIGURE 10: RCS measurements with multiple target geometries, distances and frequencies. The measurements and the theoretical RCSs are respectively represented by solid and dashed lines, or by crosses and dots in Figure 10f.

compared with the theoretical model of (64). Less than 0.5 dB of error is achieved for the MSP. Though, for the other square plates, higher discrepancies are observed. On the one hand, for the SSP, the RCS is overestimated, owing to the residual clutter after imperfect cancellation, which is not negligible w.r.t. the useful reflection from the target. Additionally, these differences can also be explained by the difficulty to calibrate the positions and orientations of the antennas and target. On the other hand, the RCS is also overestimated for the LSP. First, the introduction of the large target on the scene modifies consequently the clutter response, reducing the efficiency of the clutter cancellation. Then, the intensity of the radar echo being high, additional reflections of the radar echo on the environment are received at the antenna. For the sphere and the cylinder, the results obtained for curved plates are not accurate owing to the high curvature radii of the targets, compared to the considered distances. Additionally, the sphere is only approximated by a curved rectangular plate.

Nevertheless, one can observe that the RCS is nearly independent of the distance for the SSP, MSP, and the sphere, whereas it increases with the distance for the LSP and the cylinder. The Fraunhofer distances varies from 27 cm to 38 cm for the SSP, and from 107 cm to 153 cm for the MSP. Thus, owing to the considered distances, this happens in accordance with the theoretical models.

VI. CONCLUSION

In this paper, new radar propagation and RCS models based on the EM theory have been developed. The targets are modelled as flat square and curved rectangular plates. For the flat square plate geometry, the model is valid both for near- and far-field propagations. It analytically links the GO approximation used in ray-tracing applications, and the radar equation. For the curved rectangular plate geometry, the model enables to approximate the response of many arbitrary shapes, including cylinder, sphere and paraboloids. These models have been compared numerically and with RCS measurements for multiple targets. The results highlight the variation of the RCS with the distance, the carrier frequency, and the target shape. Finally, these models have been applied to an automotive scenario studied within the stochastic geometry framework, in order to evaluate the impact of the different models on the average sensing performance. It has been shown that the model should be chosen adequately w.r.t. the scenario to evaluate accurately the radar performance, as high differences are observed depending on the RCS modelling.

In future works, additional measurements could be performed to improve the matching between theoretical and experimental results. For instance, the actual configuration is quasi-monostatic, and the model may be corrected to take into account the angle between the antennas, and the total travelled distance. Additionally, RCS measurements of realistic targets, e.g. the back of a real vehicle, may be carried out, to evaluate at which extent the models developed for simple target are able to predict the evolution of the RCS with the distance and carrier frequency. Finally, the RCS model of the cylinder and sphere could be improved, increasing the robustness of the model for highly curved shapes.

REFERENCES

[1] "System reference document (SRdoc); transmission characteristics; technical characteristics for radiodetermination equipment for ground based vehicular applications within the frequency range 77 GHz to 81 GHz," *ETSI TR 103 593*, 05 2020.

[2] "5G; NR; user equipment (UE) radio transmission and reception (3GPP TS 38.101-1 version 17.5.0 release 17)," *ETSI TR 138 101-1*, 05 2020.

[3] Y. Hmamouche, M. Benjillali, S. Saoudi, H. Yanikomeroglu, and M. D. Renzo, "New Trends in Stochastic Geometry for Wireless Networks: A Tutorial and Survey," *Proceedings of the IEEE*, vol. 109, no. 7, pp. 1200–1252, 2021.

[4] F. Baccelli and B. Blaszczyszyn, *Stochastic Geometry and Wireless Networks: Volume I Theory*. 2010.

[5] F. Baccelli and B. Blaszczyszyn, *Stochastic Geometry and Wireless Networks: Volume II Applications*. 2010.

[6] S. Aditya, O. Dizdar, B. Clerckx, and X. Li, "Sensing using coded communications signals," *IEEE Open Journal of the Communications Society*, vol. 4, pp. 134–152, 2023.

[7] C. Aydogdu, M. F. Keskin, and H. Wymeersch, "Automotive radar interference mitigation via multi - hop cooperative radar communications," in *2020 17th European Radar Conference (EuRAD)*, pp. 270–273, 2021.

[8] H. Friis, "A note on a simple transmission formula," *Proceedings of the IRE*, vol. 34, no. 5, pp. 254–256, 1946.

[9] M. A. Richards, *Fundamentals of Radar Signal Processing*. McGraw-Hill Professional, 2005.

[10] Z. Yun and M. F. Iskander, "Ray tracing for radio propagation modeling: Principles and applications," *IEEE Access*, vol. 3, pp. 1089–1100, 2015.

[11] A. Munari, L. Simic, and M. Petrova, "Stochastic geometry interference analysis of radar network performance," *IEEE Communications Letters*, vol. 22, no. 11, pp. 2362–2365, 2018.

[12] J. Park and R. W. H. Jr, "Analysis of Blockage Sensing by RADARs in Random Cellular Networks," *IEEE Signal Processing Letters*, vol. 25, no. 11, pp. 1620–1624, 2018.

[13] S. S. Ram, G. Singh, and G. Ghatak, "Optimization of Radar Parameters for Maximum Detection Probability Under Generalized Discrete Clutter Conditions Using Stochastic Geometry," *IEEE Open Journal of Signal Processing*, vol. 2, pp. 571–585, 2021.

[14] S. S. Ram and G. Ghatak, "Estimation of Bistatic Radar Detection Performance Under Discrete Clutter Conditions Using Stochastic Geometry," 2022.

[15] Z. Fang, Z. Wei, X. Chen, H. Wu, and Z. Feng, "Stochastic geometry for automotive radar interference with RCS characteristics," *IEEE Wireless Communications Letters*, vol. 9, no. 11, pp. 1817–1820, 2020.

[16] P. Chu, J. A. Zhang, X. Wang, Z. Fei, G. Fang, and D. Wang, "Interference Characterization and Power Optimization for Automotive Radar with Directional Antenna," *IEEE Transactions on Vehicular Technology*, vol. 69, no. 4, pp. 3703–3716, 2020.

[17] Z. Fang, Z. Wei, H. Ma, X. Chen, and Z. Feng, "Analysis of Automotive Radar Interference among Multiple Vehicles," *2020 IEEE Wireless Communications and Networking Conference Workshops, WCNCW 2020 - Proceedings*, 2020.

[18] A. Al-Hourani, R. J. Evans, S. Kandeepan, B. Moran, and H. Eltom, "Stochastic Geometry Methods for Modeling Automotive Radar Interference," *IEEE Transactions on Intelligent Transportation Systems*, vol. 19, no. 2, pp. 333–344, 2018.

[19] L. Kui, S. Huang, and Z. Feng, "Interference analysis for automotive radar using matern hard-core point process," in *2021 IEEE/CIC International Conference on Communications in China (ICCC)*, pp. 817–822, 2021.

[20] K. V. Mishra, B. Shankar M. R., and B. Ottersten, "Stochastic-Geometry-Based Interference Modeling in Automotive Radars Using Matérn Hard-Core Process," *IEEE National Radar Conference - Proceedings*, vol. 2020-Septe, 2020.

[21] G. Ghatak, S. S. Kalamkar, Y. Gupta, and S. Sharma, "A Fine-Grained Analysis of Radar Detection in Vehicular Networks," vol. 9545, no. c, pp. 01–06, 2022.

[22] G. Ghatak, S. Kalamkar, and Y. Gupta, "Radar detection in vehicular networks: Fine-grained analysis and optimal channel access," *IEEE Transactions on Vehicular Technology*, pp. 1–1, 2022.

[23] H. Ma, Z. Wei, X. Chen, Z. Fang, Y. Liu, F. Ning, and Z. Feng, "Performance analysis of joint radar and communication enabled vehicular ad hoc network," *2019 IEEE/CIC International Conference on Communications in China, ICCC 2019*, no. Iccc, pp. 887–892, 2019.

[24] D. Ghozlani, A. Omri, S. Bouallegue, H. Chamkhia, and R. Bouallegue, "Stochastic Geometry-based Analysis of Joint Radar and Communication-Enabled Cooperative Detection Systems," pp. 325–330, 2021.

[25] J. Taylor and A. Terzuoli, "On the concept of near field radar cross section," in *IEEE Antennas and Propagation Society International Symposium 1997. Digest*, vol. 2, pp. 1172–1175 vol.2, 1997.

[26] P. Pouliguen and L. Desclos, "A physical optics approach to near field RCS computations," in *Annales des télécommunications*, vol. 51, pp. 219–226, 1996.

[27] P. Pouliguen, J. F. Damiens, R. Hemon, and J. Saillard, "RCS computation in near field," in *DAYS on DIFFRACTION 2006*, pp. 252–265, 2006.

[28] S. Legault, "Refining physical optics for near-field computations," *Electronics Letters*, vol. 40, no. 1, p. 1, 2004.

[29] R. Deban, H. Boutayeb, J. Conan, and K. Wu, "Numerical and experimental analysis of metallic plate near-field RCS at oblique incidence and applications to radar systems," in *2009 Loughborough Antennas & Propagation Conference*, pp. 441–444, 2009.

[30] R. Deban, H. Boutayeb, K. Wu, and J. Conan, "Deterministic approach for spatial diversity analysis of radar systems using near-field radar cross section of a metallic plate," *IEEE Transactions on Antennas and Propagation*, vol. 58, no. 3, pp. 908–916, 2010.

[31] J. M. Tamayo-Palau and P. de Resseguier, "Simulation of near field RCS to reproduce measurement condition," in *2018 15th European Radar Conference (EuRAD)*, pp. 103–106, 2018.

[32] H.-T. Chou, W.-J. Gao, J. Zhou, B. You, and X.-H. He, "Enhancing electromagnetic backscattering responses for target detection in the near zone of near-field-focused phased array antennas," *IEEE Transactions on Antennas and Propagation*, vol. 69, no. 3, pp. 1658–1669, 2021.

[33] A. Elfrgani and C. J. Reddy, "Near-field RCS for automotive radar applications," in *2019 International Workshop on Antenna Technology (iWAT)*, pp. 217–220, 2019.

[34] H.-T. Chou, "Near-field orthogonal beam scan by phased arrays of antennas with active analog beamformer for maximum NF-RCS in target detection," *IEEE Transactions on Antennas and Propagation*, vol. 70, no. 2, pp. 1559–1564, 2022.

[35] A. Lahuerta-Lavieja, M. Johansson, U. Gustavsson, T. A. H. Bressner, and G. A. E. Vandenbosch, "Computationally efficient millimeter-wave backscattering models: A single-scattering model," *IEEE Transactions on Antennas and Propagation*, vol. 68, no. 8, pp. 6306–6316, 2020.

[36] A. Lahuerta-Lavieja, M. Johansson, C. Larsson, U. Gustavsson, and G. A. E. Vandenbosch, "Computationally efficient millimeter-wave scattering models: A multiple-scattering model," *IEEE Transactions on Antennas and Propagation*, vol. 70, no. 9, pp. 8250–8261, 2022.

[37] V. A. Borovikov, "Uniform stationary phase method," *Institution of Electrical Engineers*, 1994.

[38] M. Abramowitz, *Handbook of Mathematical Functions, With Formulas, Graphs, and Mathematical Tables,*. USA: Dover Publications, Inc., 1974.

[39] J. B. Andersen, "Fresnel zones for ground-based antennas," *IEEE Transactions on Antennas and Propagation*, vol. 12, pp. 417–422, 1964.

[40] F. Miller, A. Vandome, and J. McBrewster, *Fermat's Theorem (Stationary Points): Theorem, Real Analysis, Pierre de Fermat, Maxima and Minima, Derivative, Open Set, Stationary Point, Equation, Necessary and Sufficient Condition, Inflection Point, Second Derivative*. Alphascript Publishing, 2009.

[41] P. Swerling, "Probability of detection for fluctuating targets," *IRE Transactions on Information Theory*, vol. 6, no. 2, pp. 269–308, 1960.

FRANCOIS DE SAINT MOULIN received the B.Sc. and the M.Sc. degrees in 2018 and 2020, respectively, in electrical engineering from the Université catholique de Louvain, (UCLouvain), Louvain-la-Neuve, Belgium, where he is currently working toward the Ph.D. degree with the Institute for Information and Communication Technologies, Electronics and Applied Mathematics, (ICTEAM), UCLouvain. His research interests include integrated sensing and communication technologies, near-field channel modelling and signal processing for radar and communication, and stochastic geometry.

KHALDOUN AL KHALIFEH was born in Aleppo, Syria. He received the Diploma in Electrical and Electronic Engineering, from Aleppo University-Faculty of Electrical and Electronic Engineering, in 2006, and the Master degree in Microwave and Telecommunication from the Université catholique de Louvain (UCLouvain), Belgium, in 2010. From 2011 to 2017, he worked as a research assistant with the Antenna Research Group, Institute of Information and Communication Technologies, Electronics and Applied Mathematics (ICTEAM), UCLouvain. On March 2017, he received the Ph.D. degree in applied sciences from UCLouvain. From mars 2017 to June 2023, he was involved as a post-doctoral researcher at UCLouvain. He is now an antenna and over-the-air testing leader at eV Technologies. His research interests include multi-band antenna array design and analysis, space application, fast numerical methods for electromagnetic fields in finite periodic structures, near-field imaging, thermal measurements, industrial testing and meta-surface antennas.

CHRISTOPHE CRAEYE (Senior Member, IEEE) received the M.S. degree in electrical engineering and the Ph.D. degree in microwave remote sensing from the Université catholique de Louvain (UCLouvain), Louvain-la-Neuve, Belgium, in 1994 and 1998, respectively.,From 1999 to 2001, he stayed as a Post-Doctoral Researcher in The Netherlands, in the framework of the Square Kilometer Array radio telescope project. He is currently a Professor at UCLouvain. His research topics are multiple-antenna systems and metamaterials.,Dr. Craeye served as an associate editor for several IEEE journals from 2004 to 2017.

LUC VANDENDORPE (Fellow, IEEE) was born in Mouscron, Belgium, in 1962. He received the degree (summa cum laude) in electrical engineering and the Ph.D. degree in applied science from UCLouvain, Louvain-la-Neuve, Belgium, in 1985 and 1991, respectively. Since 1985, he has been with the Communications and Remote Sensing Laboratory, UCL, where he first worked in the field of bit rate reduction techniques for video coding. In 1992, he was a Visiting Scientist and a Research Fellow with the Telecommunications and Traffic Control Systems Group, Delft Technical University, The Netherlands, where he worked on spread spectrum techniques for personal communications systems. From October 1992 to August 1997, he was a Senior Research Associate with the Belgian NSF, UCL, and an invited Assistant Professor. He is currently a Full Professor with the Institute for Information and Communication Technologies, Electronics and Applied Mathematics, UCLouvain. His research interests include digital communication systems and more precisely resource allocation for OFDM(A)-based multicell systems, MIMO and distributed MIMO, sensor networks, UWB-based positioning, and wireless power transfer. He is or has been a TPC Member for numerous IEEE conferences, such as VTC, GLOBECOM, SPAWC, ICC, PIMRC, and WCNC. He was an Elected Member of the Signal Processing for Communications Committee from 2000 to 2005 and the Sensor Array and Multichannel Signal Processing Committee of the Signal Processing Society from 2006 to 2008 and from 2009 to 2011. He was the Chair of the IEEE Benelux Joint Chapter on communications and vehicular technology from 1999 to 2003. He was the Co-Technical Chair of IEEE ICASSP 2006. He served as an Editor of synchronization and equalization for IEEE TRANSACTIONS ON COMMUNICATIONS from 2000 to 2002 and as an Associate Editor for IEEE TRANSACTIONS ON WIRELESS COMMUNICATIONS from 2003 to 2005 and IEEE TRANSACTIONS ON SIGNAL PROCESSING from 2004 to 2006.

CLAUDE OESTGES (Fellow, IEEE) received the M.Sc. and Ph.D. degrees in Electrical Engineering from UCLouvain, Louvain-la-Neuve, Belgium, respectively in 1996 and 2000. In January 2001, he joined as a post-doctoral scholar the Smart Antennas Research Group (Information Systems Laboratory), Stanford University, CA, USA. From January 2002 to September 2005, he was associated with the Microwave Laboratory UCLouvain as a post-doctoral fellow of the Belgian Fonds de la Recherche Scientifique (FRS-FNRS). Claude Oestges is presently Full Professor with the Electrical Engineering Department, Institute for Information and Communication Technologies, Electronics and Applied Mathematics (ICTEAM), UCLouvain. He is the author or co-author of four books and more than 200 journal papers and conference communications, and he was the chair of COST Action CA15104 IRACON (2016-2020), as well as the recipient of the 1999-2000 IET Marconi Premium Award and of the IEEE Vehicular Technology Society Neal Shepherd Award in 2004 and 2012.